

Honeycomb supersolid – Dirac points and shear-instability induced crystal transitions

P. B. Blakie 

*Dodd-Walls Centre for Photonic and Quantum Technologies, Dunedin 9054, New Zealand and
Department of Physics, University of Otago, Dunedin 9016, New Zealand*

(Dated: October 22, 2024)

The honeycomb supersolid state is predicted to form in a dipolar Bose-Einstein condensate with a planar confining potential. Our results for its excitation spectrum reveal the gapless bands and the emergence of Dirac points at the Brillouin zone edge, manifesting as points where the second sound and transverse sound bands touch. The honeycomb supersolid has three sound speeds that we connect to its elastic parameters through hydrodynamic theory. From this analysis we find conditions where a shear instability occurs as the honeycomb rigidity disappears. This gives insight into the nonequilibrium dynamics following an interaction quench, where the honeycomb pattern melts and different crystal orders emerge.

A two-dimensional (2D) triangular supersolid has been realized using a dipolar Bose-Einstein condensate (BEC) confined in a trapping potential with an oblate shape [1, 2]. This system exhibits a complex phase diagram, featuring various ground-state crystal patterns, separated by first-order phase transitions [3–8]. One of the intriguing phases that emerges is the honeycomb-patterned supersolid, which combines high modulational contrast with a significant superfluid fraction [3, 9]. Experimental developments, such as the production of larger dipolar condensates [10, 11] and progress with polar molecule condensates [12, 13], should soon lead to the experimental realization of honeycomb supersolids.

Honeycomb lattices garnered considerable interest following studies on graphene [14, 15]. In graphene the band structure exhibits degeneracies where two bands touch at the corners of the first Brillouin zone, known as the Dirac points. Near the Dirac points, the excitation bands take on a cone-like shape, akin to massless relativistic particles. Cold-atom systems have been used to engineer similar band structures with the honeycomb structure imposed externally by optical lattices [16–30]. A honeycomb supersolid is unique because its lattice structure emerges spontaneously and coexists with superfluidity. As a result of these multiple broken symmetries, a 2D supersolid is expected to exhibit three gapless excitation bands associated with Nambu-Goldstone modes [31].

In this paper, we present the first results for the excitation spectrum of the honeycomb supersolid. The three lowest excitation bands can be characterized as longitudinal first and second sound, as well as a transverse sound. These excitations are dominated by the incompressible nature of the dipolar system, causing the speed of first sound (crystal modes) to be much higher than the other two sounds. Our results show that Dirac points emerge in the lowest two sound branches.

We also explore the behavior of the sound speeds and elastic parameters as the contact interaction (a_s) is varied across the transition to the stripe-patterned supersolid phase. Here we find that the honeycomb state remains metastable until the shear modulus (and transverse speed of sound) eventually vanishes, signalling the loss of crystal rigidity. These conclusions are validated through non-equilibrium simulations, demonstrating this instability can cause a transition to states with stripe, triangular and mixed crystalline order. Intriguingly, phase coherence can persist during these crystal transitions.

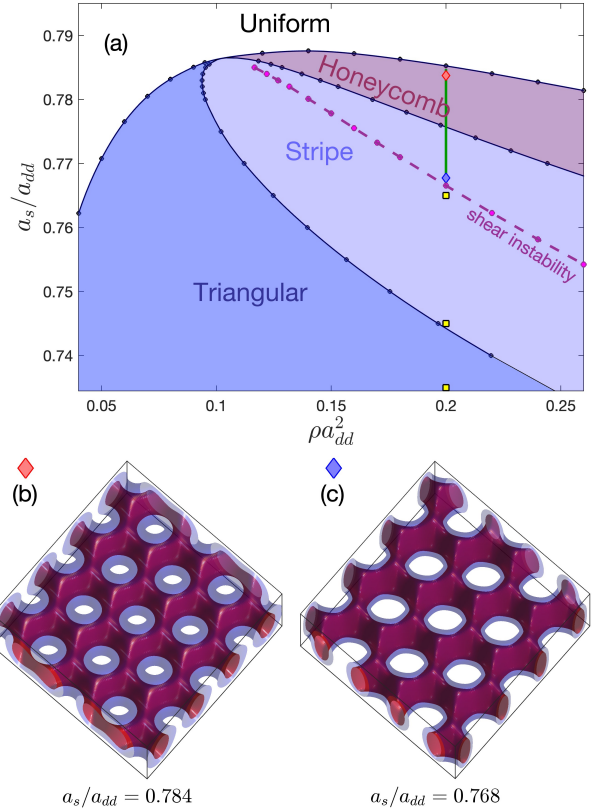


FIG. 1. (a) Ground state phase diagram for a planar dipolar BEC of ^{164}Dy . Boundaries determined by finding where adjacent phases are degenerate (blue circles). Green line shows the parameter regime in Fig. 3 and the dashed magenta line shows where the honeycomb state becomes unstable. Yellow squares indicate quench parameters [see Fig. 4]. (b), (c) Example honeycomb ground states with parameters indicated by diamond markers in (a) and plotted in a cubic region of side length $20\ \mu\text{m}$. Red (blue) colored isosurfaces are at a density of $3 \times 10^{20}\ \text{m}^{-3}$ ($1.5 \times 10^{20}\ \text{m}^{-3}$).

Formalism – We present results for the case of a dipolar BEC of highly magnetic ^{164}Dy atoms with magnetic dipole moments polarized along z and in a planar trap with axial harmonic confinement of angular frequency $\omega_z/2\pi = 72.4\ \text{Hz}$. These atoms have a short ranged interaction with s -wave scat-

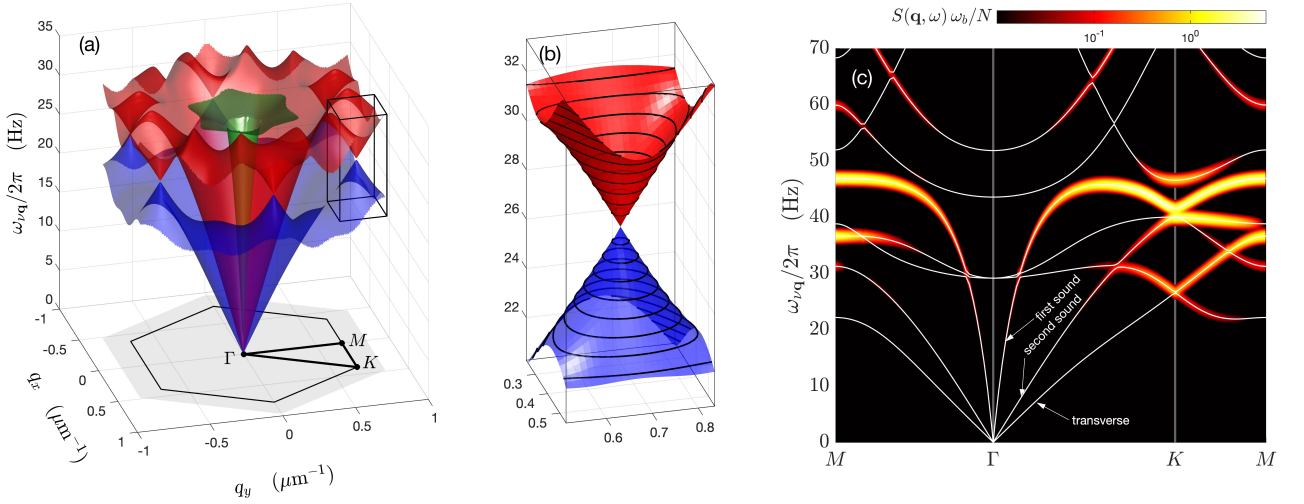


FIG. 2. Band structure of a honeycomb supersolid. (a) Lowest three excitations bands. The symmetry points $\{\Gamma, M, K\}$ and the first Brillouin zone are indicated for reference. (b) Close up of Dirac cones near the K -point [range indicated by rectangular cuboid in (a)]. (c) Excitations along the three symmetry directions of the Brillouin zone: $\hbar\omega_{\nu\mathbf{q}}$ (white lines) on a heat map image of $S(\mathbf{q}, \omega)$ [frequency broadened by $\omega_b = 10^{-2}\omega_z$, with N the atom number in the quantization volume (see Ref. [32])]. Results for $\rho = 0.2/a_{dd}^2$ and $a_s/a_{dd} = 0.780$.

tering length a_s that can be adjusted with Feshbach resonances [33], and a long-ranged dipole-dipole interaction with dipole length $a_{dd} = m\mu_0\mu_m^2/12\pi\hbar^2 = 130.8 a_0$, where $\mu_m = 10\mu_B$ is the magnetic moment and a_0 is the Bohr radius. The extended meanfield theory energy functional is

$$E = \int d\mathbf{x} \psi^* \left(h_{\text{sp}} + \frac{1}{2}\Phi + \frac{2}{5}\gamma_{\text{QF}}|\psi|^3 \right) \psi, \quad (1)$$

where $h_{\text{sp}} = -\frac{\hbar^2}{2m}\nabla^2 + \frac{1}{2}m\omega_z^2 z^2$ is the single particle Hamiltonian. Here $\Phi(\mathbf{x}) = \int d\mathbf{x}' U(\mathbf{x} - \mathbf{x}')|\psi(\mathbf{x}')|^2$ describes the two-body interactions, with the interaction potential

$$U(\mathbf{r}) = \frac{4\pi a_s \hbar^2}{m} \delta(\mathbf{r}) + \frac{3a_{dd}\hbar^2}{mr^3} \left(1 - 3\frac{z^2}{r^2} \right). \quad (2)$$

Quantum fluctuation effects are important when the dipolar interactions dominate ($a_s/a_{dd} < 1$) and stabilise the condensate from mechanical collapse [34–38]. The quantum fluctuation term has coefficient $\gamma_{\text{QF}} = 128\hbar^2\sqrt{\pi a_s^3} Q_5(a_{dd}/a_s)/3m$, where $Q_5(x) = \Re\{\int_0^1 du [1 + x(3u^2 - 1)]^{5/2}\}$ [39, 40].

Phase diagram – The phase diagram presented in Fig. 1(a) characterizes the ground state as a function of average areal density ρ and interaction parameter ratio a_s/a_{dd} . This is determined by solving for the stationary states of the energy functional, which satisfy the extended Gross-Pitaevskii equation (eGPE) $\mu\psi = \mathcal{L}\psi$, where $\mathcal{L} \equiv h_{\text{sp}} + \Phi + \gamma_{\text{QF}}|\psi|^3$, and μ is the chemical potential. The average density constraint is enforced through the normalization condition $\int_{\text{uc}} d\mathbf{x} |\psi(\mathbf{x})|^2 = \rho A_{\text{uc}}$, where A_{uc} is the unit cell area and the integration is taken over a unit cell of the periodic density pattern. Depending on the parameters the condensate can prefer to be in a uniform superfluid state or a spatially modulated state of various crystal structures (see Refs. [3, 8, 41–43] for de-

tails of these calculations). We show two examples of honeycomb ground states in Figs. 1(b) and (c). The connected “rings” of the honeycomb state confer a high superfluid fraction [3, 8, 44] relative to the triangular ground state (and related one-dimensional dipolar supersolids), where the unit cell is dominated by localized droplet-like states, and tunnelling between to neighboring sites is highly suppressed. The transitions between states are generally first-order, e.g. see the Fig. 3(a), where an abrupt change in the contrast (density modulation) and the superfluid fraction occurs at the uniform to honeycomb transition point.

Excitation spectrum – The collective excitations of the supersolid are determined by solving the extended Bogoliubov-De Gennes (BdG) equations [45]: $H\mathbf{w}_{\nu\mathbf{q}} = \hbar\omega_{\nu\mathbf{q}}\mathbf{w}_{\nu\mathbf{q}}$, where

$$H = \begin{bmatrix} \mathcal{L} + X - \mu & -X \\ X & -(\mathcal{L} + X - \mu) \end{bmatrix}, \quad (3)$$

with $\mathbf{w}_{\nu\mathbf{q}} = [u_{\nu\mathbf{q}}, v_{\nu\mathbf{q}}]^T$ and $\{\hbar\omega_{\nu\mathbf{q}}\}$ being the excitation modes and energies, respectively. Here $\mathbf{q} = (q_x, q_y)$ is the quasimomentum, ν is the band index and

$$Xf = \psi(\mathbf{x}) \int d\mathbf{x}' U(\mathbf{x} - \mathbf{x}') f(\mathbf{x}') \psi^*(\mathbf{x}') + \frac{3}{2}\gamma_{\text{QF}}|\psi|^3 f. \quad (4)$$

We give results for the honeycomb excitation spectrum in Fig. 2. As expected for a 2D supersolid, the lowest three-excitation bands are gapless [31]. These arise from the Nambu-Goldstone modes associated with broken phase symmetry and the broken 2D translational symmetry. The lowest excitation band is a transverse excitation, and the higher two are longitudinal excitations referred to first and second sound [see Fig. 2(c)]. Second sound manifests from the normal fraction arising from the broken translational invariance [46]. The lowest three bands are shown over the first Brillouin zone in Fig. 2(a). The band structure is observed to have 6 Dirac

points at the edge of the Brillouin zone. At these points the lowest two bands are degenerate and close by the dispersion of these bands is linear (cone like) [see Fig. 2(b)].

The band structure along the symmetry lines is shown in Fig. 2(c). Here we also display the dynamic structure factor

$$S(\mathbf{q}, \omega) = \sum_{\nu} \left| \int d\mathbf{x} (u_{\nu\mathbf{q}}^* - v_{\nu\mathbf{q}}^*) e^{i\mathbf{q}\cdot\mathbf{x}\psi} \right|^2 \delta(\omega - \omega_{\nu\mathbf{q}}), \quad (5)$$

which characterizes the density fluctuations in the system and demonstrates how strongly the various excitation branches respond to a density coupled probe [32]. Except near the Brillouin zone edges, most of the weight of $S(\mathbf{q}, \omega)$ is from the first sound mode (which crosses 3rd band near Γ to be the 5th band near M and K). The lowest two bands near the Dirac points develop significant weight indicating that this feature will be susceptible to probing.

Speeds of sound – The speeds of sound can be determined from the slope of the lowest three bands near the Γ point. These are shown as function of a_s in Fig. 3(b). These results take a slice through the phase diagram crossing into the stripe state phase (i.e. honeycomb is metastable) [see Fig. 1(a)]. In this metastable regime the transverse speed of sound softens to zero marking a shear instability. We also note that the first sound speed is much higher than the other sounds. A relatively high first sound speed is also found for one-dimensional and the triangular 2D dipolar supersolids [42, 47–49].

Elastic parameters – We can define elastic parameters from understanding how the ground state energy density \mathcal{E} (i.e. energy per area) changes with the average density ρ and the lattice constants describing the crystal periodicity. This introduces the parameters $\{\alpha_{\rho\rho}, \alpha_{uu}, \alpha_{\rho u}, \tilde{\mu}\}$ that appear in the superfluid hydrodynamic theory. The first parameter, $\alpha_{\rho\rho} \equiv \frac{\partial^2 \mathcal{E}}{\partial \rho^2}$, relates to the isothermal compressibility at constant strain $\tilde{\kappa} = (\rho^2 \alpha_{\rho\rho})^{-1}$. The honeycomb lattice has an isotropic elastic tensor [50] characterized by the Lamé parameters $\{\tilde{\lambda}, \tilde{\mu}\}$, with $\tilde{\mu}$ being the shear modulus. The longitudinal modulus, $\alpha_{uu} \equiv \tilde{\lambda} + 2\tilde{\mu}$, is the diagonal element of the elastic tensor. We also evaluate density-strain coupling parameter $\alpha_{\rho u}$, which quantifies the mixed derivative of \mathcal{E} with respect to changes in density and cell area, although this tends to be small. The elastic parameters are calculated from ground state solutions using finite differences in ρ and unit cell distortion, and are shown in Fig. 3(c) (e.g. see Refs. [42, 51, 52]).

The hydrodynamic theory [42, 51, 53] relates the speeds of sound to the elastic parameters as

$$m c_{\pm}^2 = \varepsilon \pm \sqrt{\varepsilon^2 - \frac{\rho_s}{\rho_n} (\alpha_{\rho\rho} \alpha_{uu} - \alpha_{\rho u}^2)}, \quad c_t = \sqrt{\frac{\tilde{\mu}}{\rho_n}}, \quad (6)$$

being first (c_+), second (c_-) and transverse (c_t) sound, respectively, where we have set $\varepsilon = (\rho \alpha_{\rho\rho} - 2\alpha_{\rho u} + \alpha_{uu}/\rho_n)/2$. Here $\rho_n = (1 - f_s)\rho$ and $\rho_s = f_s\rho$ are the normal and superfluid density, respectively, where f_s is the supersolid fraction. The speeds of sound determined by the BdG and hydrodynamic calculations are in good agreement [Fig. 3(c)]. As expected from Eq. (6), $c_t \rightarrow 0$ at the shear instability due to $\tilde{\mu}$ vanishing. This signals the honeycomb lattice losing rigidity.

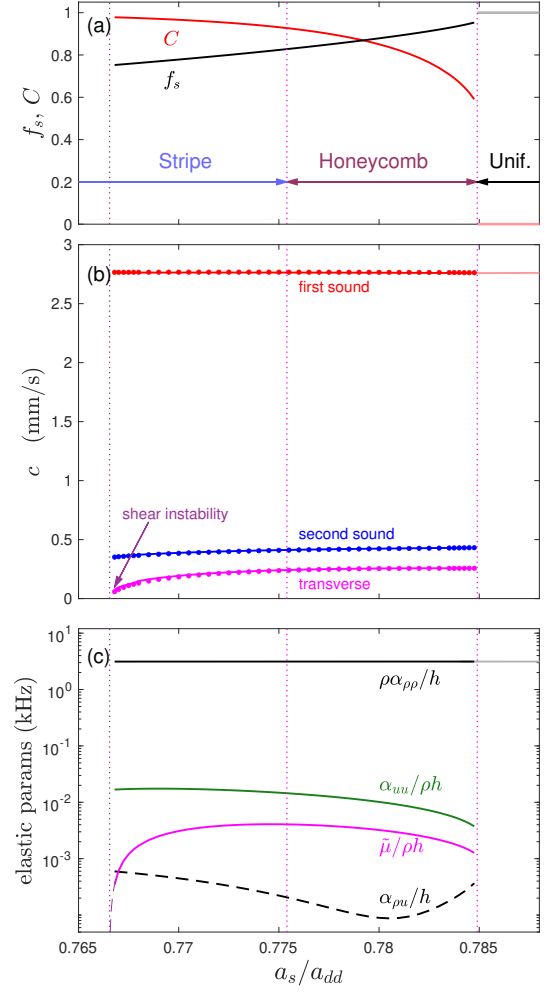


FIG. 3. Speeds of sounds and elastic parameters of honeycomb supersolid. (a) Superfluid fraction f_s and the planar density contrast C of the honeycomb state. Also shown for the uniform state where it is the ground state (lightly colored lines). Labels indicate where the uniform, honeycomb and stripe are the ground states with vertical dotted lines indicating the transitions. (b) Speeds of sound from BdG calculations (lines) and hydrodynamic result (dots). Uniform superfluid result (light solid line). (c) Elastic parameters (solid and dashed lines), with $\alpha_{\rho\rho}$ for the uniform state (light solid line). Polynomial extrapolation determining instability point (dashed magenta line) where $c_t, \tilde{\mu} \rightarrow 0$. The superfluid fraction is isotropic and calculated as in Ref. [44], and $C = (\varrho_{\max} - \varrho_{\min})/(\varrho_{\max} + \varrho_{\min})$, where ϱ_{\max} (ϱ_{\min}) is the maximum (minimum) of the areal density. The parameters for these results are the green line in Fig. 1(a).

Extending this analysis to other densities we determine the instability boundary on the phase diagram [Fig. 1(a)]. Above this line the honeycomb state is dynamically stable. It would be interesting to extend this line to the critical point, where all 4 phases meet, however the density contrast vanishes as we approach the critical point and a careful analysis of the shear instability in this region is difficult.

Quench dynamics – We explore the metastability and instabilities of the honeycomb supersolid with the dynamics fol-

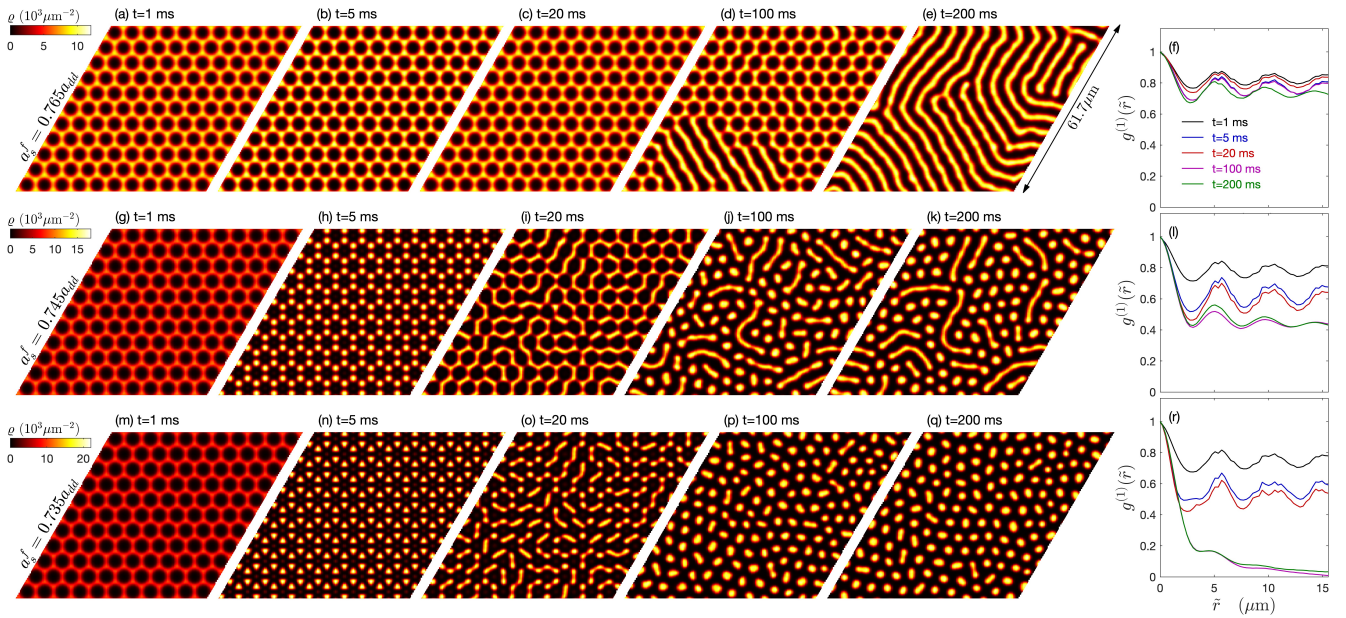


FIG. 4. Dynamics of a honeycomb supersolid following a quench into the unstable regime. Areal density ρ and coherence evolution for quenches to (a)-(f) $a_s^f = 0.765a_{dd}$, (g)-(l) $a_s^f = 0.745a_{dd}$, and (m)-(r) $a_s^f = 0.735a_{dd}$ [final parameters shown on Fig. 1(a)]. Initial state for $a_s = 0.770 a_{dd}$ [Fig. 1(c)] with noise added. Coherence function $g^{(1)}(\vec{r}) = G(\vec{r})/G(0)$, where $G(\vec{r})$ is the angular average of the correlation function $G(\vec{r}) = \frac{1}{A} \int d\vec{r}' \psi^*(\vec{r}' + \vec{r}) \psi(\vec{r}')$, with $\vec{r}' = (x, y, 0)$ and A being the system area. Quench parameters indicated in Fig. 1.

lowing an a_s quench. We perform simulations of finite sample of 11×11 cells (system in a right rhombic prism shaped spatial region) with periodic boundary conditions on the xy -plane boundaries. The initial state is the metastable honeycomb state at $a_s^i/a_{dd} = 0.768$ [Fig. 1(c)] with white noise added (increasing the energy by $\sim 5\%$) to simulate the effects of quantum and thermal fluctuations, which play an important role in seeding instabilities [54]. This initial state is evolved using the truncated Wigner method (see [54, 55]) with the a_s quenched to the final value a_s^f at $t = 0$. We present three example trajectories in Fig. 4 for different values of a_s^f . Generically the quench excites a breathing oscillation where the peak density and width of the honeycomb walls oscillate with a period of ~ 10 ms [e.g. see Figs. 4(a) and (b)]. If a_s^f is above the shear instability, the oscillation continues for the duration of simulation without any degradation of the honeycomb structure. For values of a_s^f below the instability, the honeycomb structure breaks down and the system reorganizes. For the quench in Figs. 4(a)-(e) a disordered stripe-like pattern starts forming at $t \sim 100$ ms. This decay happens more rapidly for lower a_s^f , but also the final pattern changes. For values of a_s^f in the triangular region of the phase diagram [Figs. 4(m)-(q)] a triangular pattern emerges, and for a value between these two cases a mixed stripe-triangular arrangement develops [Figs. 4(g)-(k)] (cf. intriguing metastable states found in the middle of the stripe phase in Ref. [58]). In subplots (f), (l) and (r) we consider the evolution of the phase coherence. This reveals that final states with some stripe component can maintain a high phase coherence ($\gtrsim 50\%$), and can be expected to

exhibit a high superfluid rigidity.

Outlook and Conclusions – In this paper, we have analyzed the excitations of a honeycomb supersolid revealing the general behavior of sound, and the occurrence of Dirac points. Schemes for performing band spectroscopy on dipolar supersolids have been proposed and implemented in experiments [49, 56, 57] and our results show that the Dirac cones will respond to such density-coupled probes. Considering the behavior across the phase diagram, we observe that the honeycomb state is metastable over a significant portion of the stripe phase region [58] until a shear instability manifests. This can be compared to the vanishing of shear associated with the (finite-temperature) melting of a solid-state crystal [59]. Also, it has been found that thermal effects can modify the dipolar supersolid phase diagram [60, 61], suggesting the extension of our study to finite temperature is of interest.

We have presented non-equilibrium simulations exploiting this instability, showing how a_s quenches lead to the honeycomb crystal melting into stripe, triangular and mixed phases on time-scales accessible to experiments. These types of quenches will be suitable for mapping out the phase diagram, verifying metastability, and open new directions for studying nonequilibrium dynamics of transitions between different types of supersolids. The planar results we consider provide a general understanding of dipolar BECs prepared in pancake-shaped traps, but will be more closely realized in experiments employing optical box traps [62].

Acknowledgments – The New Zealand eScience Infrastructure (NeSI) and support from the Marsden Fund of the Royal Society of New Zealand.

- [1] M. A. Norcia, C. Politi, L. Klaus, E. Poli, M. Sohmen, M. J. Mark, R. N. Bisset, L. Santos, and F. Ferlaino, Two-dimensional supersolidity in a dipolar quantum gas, *Nature* **596**, 357 (2021).
- [2] T. Bland, E. Poli, C. Politi, L. Klaus, M. A. Norcia, F. Ferlaino, L. Santos, and R. N. Bisset, Two-dimensional supersolid formation in dipolar condensates, *Phys. Rev. Lett.* **128**, 195302 (2022).
- [3] Y.-C. Zhang, F. Maucher, and T. Pohl, Supersolidity around a critical point in dipolar Bose-Einstein condensates, *Phys. Rev. Lett.* **123**, 015301 (2019).
- [4] E. Poli, T. Bland, C. Politi, L. Klaus, M. A. Norcia, F. Ferlaino, R. N. Bisset, and L. Santos, Maintaining supersolidity in one and two dimensions, *Phys. Rev. A* **104**, 063307 (2021).
- [5] J. Hertkorn, J.-N. Schmidt, M. Guo, F. Böttcher, K. S. H. Ng, S. D. Graham, P. Uerlings, H. P. Büchler, T. Langen, M. Zwierlein, and T. Pfau, Supersolidity in two-dimensional trapped dipolar droplet arrays, *Phys. Rev. Lett.* **127**, 155301 (2021).
- [6] Y.-C. Zhang, T. Pohl, and F. Maucher, Phases of supersolids in confined dipolar Bose-Einstein condensates, *Phys. Rev. A* **104**, 013310 (2021).
- [7] Y.-C. Zhang and F. Maucher, Variational approaches to two-dimensionally symmetry-broken dipolar Bose-Einstein condensates, *Atoms* **11**, 102 (2023).
- [8] B. T. E. Ripley, D. Baillie, and P. B. Blakie, Two-dimensional supersolidity in a planar dipolar Bose gas, *Phys. Rev. A* **108**, 053321 (2023).
- [9] A. Gallemí and L. Santos, Superfluid properties of a honeycomb dipolar supersolid, *Phys. Rev. A* **106**, 063301 (2022).
- [10] S. Jin, J. Gao, K. Chandrashekhara, C. Götzhäuser, J. Schöner, and L. Chomaz, Two-dimensional magneto-optical trap of dysprosium atoms as a compact source for efficient loading of a narrow-line three-dimensional magneto-optical trap, *Phys. Rev. A* **108**, 023719 (2023).
- [11] M. Krstajić, P. Juhász, J. c. v. Kučera, L. R. Hofer, G. Lamb, A. L. Marchant, and R. P. Smith, Characterization of three-body loss in ^{166}Er and optimized production of large Bose-Einstein condensates, *Phys. Rev. A* **108**, 063301 (2023).
- [12] M. Schmidt, L. Lassablière, G. Quémener, and T. Langen, Self-bound dipolar droplets and supersolids in molecular Bose-Einstein condensates, *Phys. Rev. Res.* **4**, 013235 (2022).
- [13] N. Bigagli, W. Yuan, S. Zhang, B. Bulatovic, T. Karman, I. Stevenson, and S. Will, Observation of Bose-Einstein condensation of dipolar molecules, *Nature* (2024).
- [14] Y. Zhang, Y.-W. Tan, H. L. Stormer, and P. Kim, Experimental observation of the quantum Hall effect and Berry's phase in graphene, *Nature* **438**, 201 (2005).
- [15] K. S. Novoselov, A. K. Geim, S. V. Morozov, D. Jiang, M. I. Katsnelson, I. V. Grigorieva, S. V. Dubonos, and A. A. Firsov, Two-dimensional gas of massless Dirac fermions in graphene, *Nature* **438**, 197 (2005).
- [16] G. Grynberg, B. Lounis, P. Verkerk, J.-Y. Courtois, and C. Salomon, Quantized motion of cold cesium atoms in two- and three-dimensional optical potentials, *Phys. Rev. Lett.* **70**, 2249 (1993).
- [17] C. Wu, D. Bergman, L. Balents, and S. Das Sarma, Flat bands and Wigner crystallization in the honeycomb optical lattice, *Phys. Rev. Lett.* **99**, 070401 (2007).
- [18] S.-L. Zhu, B. Wang, and L.-M. Duan, Simulation and detection of Dirac fermions with cold atoms in an optical lattice, *Phys. Rev. Lett.* **98**, 260402 (2007).
- [19] M. Lewenstein, A. Sanpera, V. Ahufinger, B. Damski, A. Sen(De), and U. Sen, Ultracold atomic gases in optical lattices: mimicking condensed matter physics and beyond, *Adv. Phys.* **56**, 243 (2007).
- [20] M. J. Ablowitz, S. D. Nixon, and Y. Zhu, Conical diffraction in honeycomb lattices, *Phys. Rev. A* **79**, 053830 (2009).
- [21] K. L. Lee, B. Grémaud, R. Han, B.-G. Englert, and C. Miniatura, Ultracold fermions in a graphene-type optical lattice, *Phys. Rev. A* **80**, 043411 (2009).
- [22] A. Bermudez, N. Goldman, A. Kubasiak, M. Lewenstein, and M. A. Martin-Delgado, Topological phase transitions in the non-Abelian honeycomb lattice, *New J. Phys.* **12**, 033041 (2010).
- [23] Z. Chen and B. Wu, Bose-Einstein condensate in a honeycomb optical lattice: Fingerprint of superfluidity at the Dirac point, *Phys. Rev. Lett.* **107**, 065301 (2011).
- [24] L. H. Haddad and L. D. Carr, Relativistic linear stability equations for the nonlinear Dirac equation in Bose-Einstein condensates, *Europhys. Lett.* **94**, 56002 (2011).
- [25] P. Soltan-Panahi, J. Struck, P. Hauke, A. Bick, W. Plenkers, G. Meineke, C. Becker, P. Windpassinger, M. Lewenstein, and K. Sengstock, Multi-component quantum gases in spin-dependent hexagonal lattices, *Nature Physics* **7**, 434 (2011).
- [26] L. Tarruell, D. Greif, T. Uehlinger, G. Jotzu, and T. Esslinger, Creating, moving and merging Dirac points with a Fermi gas in a tunable honeycomb lattice, *Nature* **483**, 302 (2012).
- [27] L.-K. Lim, J.-N. Fuchs, and G. Montambaux, Bloch-Zener oscillations across a merging transition of Dirac points, *Phys. Rev. Lett.* **108**, 175303 (2012).
- [28] G. Jotzu, M. Messer, R. Desbuquois, M. Lebrat, T. Uehlinger, D. Greif, and T. Esslinger, Experimental realization of the topological Haldane model with ultracold fermions, *Nature* **515**, 237 (2014).
- [29] T. Li, L. Duca, M. Reitter, F. Grusdt, E. Demler, M. Endres, M. Schleier-Smith, I. Bloch, and U. Schneider, Bloch state tomography using Wilson lines, *Science* **352**, 1094 (2016).
- [30] N. R. Cooper, J. Dalibard, and I. B. Spielman, Topological bands for ultracold atoms, *Rev. Mod. Phys.* **91**, 015005 (2019).
- [31] H. Watanabe and T. Brauner, Spontaneous breaking of continuous translational invariance, *Phys. Rev. D* **85**, 085010 (2012).
- [32] L. Pitaevskii and S. Stringari, *Bose-Einstein Condensation and Superfluidity*, Vol. 164 (Oxford University Press, 2016).
- [33] K. Baumann, N. Q. Burdick, M. Lu, and B. L. Lev, Observation of low-field Fano-Feshbach resonances in ultracold gases of dysprosium, *Phys. Rev. A* **89**, 020701 (2014).
- [34] D. S. Petrov, Quantum mechanical stabilization of a collapsing Bose-Bose mixture, *Phys. Rev. Lett.* **115**, 155302 (2015).
- [35] I. Ferrier-Barbut, H. Kadau, M. Schmitt, M. Wenzel, and T. Pfau, Observation of quantum droplets in a strongly dipolar Bose gas, *Phys. Rev. Lett.* **116**, 215301 (2016).
- [36] F. Wächtler and L. Santos, Quantum filaments in dipolar Bose-Einstein condensates, *Phys. Rev. A* **93**, 061603(R) (2016).
- [37] R. N. Bisset, R. M. Wilson, D. Baillie, and P. B. Blakie, Ground-state phase diagram of a dipolar condensate with quantum fluctuations, *Phys. Rev. A* **94**, 033619 (2016).
- [38] L. Chomaz, I. Ferrier-Barbut, F. Ferlaino, B. Laburthe-Tolra, B. L. Lev, and T. Pfau, Dipolar physics: a review of experiments with magnetic quantum gases, *Rep. Prog. Phys.* **86**, 026401 (2022).
- [39] T. D. Lee, K. Huang, and C. N. Yang, Eigenvalues and eigenfunctions of a Bose system of hard spheres and its low-

- temperature properties, *Phys. Rev.* **106**, 1135 (1957).
- [40] A. R. P. Lima and A. Pelster, Quantum fluctuations in dipolar Bose gases, *Phys. Rev. A* **84**, 041604 (2011).
- [41] A.-C. Lee, D. Baillie, and P. B. Blakie, Numerical calculation of dipolar-quantum-droplet stationary states, *Phys. Rev. Res.* **3**, 013283 (2021).
- [42] E. Poli, D. Baillie, F. Ferlaino, and P. B. Blakie, *Excitations of a two-dimensional supersolid* (2024), arXiv:2407.01072 [cond-mat.quant-gas].
- [43] J. C. Smith, D. Baillie, and P. B. Blakie, Supersolidity and crystallization of a dipolar Bose gas in an infinite tube, *Phys. Rev. A* **107**, 033301 (2023).
- [44] P. B. Blakie, Superfluid fraction tensor of a two-dimensional supersolid, *J. Phys. B* **57**, 115301 (2024).
- [45] D. Baillie, R. M. Wilson, and P. B. Blakie, Collective excitations of self-bound droplets of a dipolar quantum fluid, *Phys. Rev. Lett.* **119**, 255302 (2017).
- [46] A. Leggett, On the superfluid fraction of an arbitrary many-body system at $T = 0$, *J. Stat. Phys.* **93**, 927 (1998).
- [47] S. M. Roccuzzo and F. Ancilotto, Supersolid behavior of a dipolar Bose-Einstein condensate confined in a tube, *Phys. Rev. A* **99**, 041601 (2019).
- [48] P. B. Blakie, L. Chomaz, D. Baillie, and F. Ferlaino, Compressibility and speeds of sound across the superfluid-to-supersolid phase transition of an elongated dipolar gas, *Phys. Rev. Res.* **5**, 033161 (2023).
- [49] M. Šindik, T. Zawislak, A. Recati, and S. Stringari, Sound, superfluidity, and layer compressibility in a ring dipolar supersolid, *Phys. Rev. Lett.* **132**, 146001 (2024).
- [50] L. D. Landau, L. P. Pitaevskii, E. M. Lifshitz, and A. M. Kosevich, *Theory of Elasticity*, 3rd ed. (Butterworth-Heinemann, 1986).
- [51] L. M. Platt, D. Baillie, and P. B. Blakie, Sound waves and fluctuations in one-dimensional supersolids, *Phys. Rev. A* **110**, 023320 (2024).
- [52] M. Rakic, A. F. Ho, and D. K. K. Lee, Elastic properties and thermodynamic anomalies of supersolids, *Phys. Rev. Res.* **6**, 043040 (2024).
- [53] C.-D. Yoo and A. T. Dorsey, Hydrodynamic theory of supersolids: Variational principle, effective lagrangian, and density-density correlation function, *Phys. Rev. B* **81**, 134518 (2010).
- [54] P. B. Blakie, A. S. Bradley, M. J. Davis, R. J. Ballagh, and C. W. Gardiner, Dynamics and statistical mechanics of ultracold Bose gases using c-field techniques, *Adv. Phys.* **57**, 363 (2008).
- [55] R. N. Bisset and P. B. Blakie, Crystallization of a dilute atomic dipolar condensate, *Phys. Rev. A* **92**, 061603 (2015).
- [56] D. Petter, A. Patscheider, G. Natale, M. J. Mark, M. A. Baranov, R. van Bijnen, S. M. Roccuzzo, A. Recati, B. Blakie, D. Baillie, L. Chomaz, and F. Ferlaino, Bragg scattering of an ultracold dipolar gas across the phase transition from Bose-Einstein condensate to supersolid in the free-particle regime, *Phys. Rev. A* **104**, L011302 (2021).
- [57] G. Biagioni, N. Antolini, B. Donelli, L. Pezzè, A. Smerzi, M. Fattori, A. Fioretti, C. Gabbanini, M. Inguscio, L. Tanzi, and G. Modugno, Measurement of the superfluid fraction of a supersolid by Josephson effect, *Nature* **629**, 773 (2024).
- [58] Y.-C. Zhang, T. Pohl, and F. Maucher, Metastable patterns in one- and two-component dipolar Bose-Einstein condensates, *Phys. Rev. Res.* **6**, 023023 (2024).
- [59] M. Born, On the stability of crystal lattices. i, *Math. Proc. Camb. Philos. Soc.* **36**, 160 (1940).
- [60] J. Sánchez-Baena, C. Politi, F. Maucher, F. Ferlaino, and T. Pohl, Heating a dipolar quantum fluid into a solid, *Nat. Commun.* **14**, 1868 (2023).
- [61] J. Sánchez-Baena, T. Pohl, and F. Maucher, Superfluid-supersolid phase transition of elongated dipolar Bose-Einstein condensates at finite temperatures, *Phys. Rev. Res.* **6**, 023183 (2024).
- [62] P. Juhász, M. Krstajić, D. Strachan, E. Gandar, and R. P. Smith, How to realize a homogeneous dipolar Bose gas in the roton regime, *Phys. Rev. A* **105**, L061301 (2022).